Direct Visualization of Conformation and Dense Packing of DNA-Based Soft Colloids

Jing Zhang,[1] Paul M. Lettinga,[1,2] Jan K. G. Dhont,[1,3] and Emmanuel Stiakakis[1,*]
[1]Forschungszentrum Jülich, Institute of Complex Systems 3, Leo-Brandt-Straße, 52425 Jülich, Germany
[2]Department of Physics and Astronomy, Laboratory for Acoustics and Thermal Physics, Katholieke Universiteit Leuven, Celestijnenlaan 200D, Leuven B-3001, Belgium
[3]Heinrich-Heine-Universität Düsseldorf, Universitätsstraße 1, 40225 Düsseldorf, Germany
(Received 6 August 2014; revised manuscript received 22 September 2014; published 31 December 2014)

Soft colloids—such as polymer-coated particles, star polymers, block-copolymer micelles, microgels—constitute a broad class of materials where microscopic properties such as deformability and penetrability of the particle play a key role in tailoring their macroscopic properties which is of interest in many technological areas. The ability to access these microscopic properties is not yet demonstrated despite its great importance. Here we introduce novel DNA-coated colloids with star-shaped architecture that allows accessing the above local structural information by directly visualizing their intramolecular monomer density profile and arm's free-end locations with confocal fluorescent microscopy. Compression experiments on a two-dimensional hexagonal lattice formed by these macromolecular assemblies reveal an exceptional resistance to mutual interpenetration of their charged corona at pressures approaching the MPa range. Furthermore, we find that this lattice, in a close packing configuration, is surprisingly tolerant to particle size variation. We anticipate that these stimuli-responsive materials could aid to get deeper insight in a wide range of problems in soft matter, including the study and design of biomimetic lubricated surfaces.

DOI: 10.1103/PhysRevLett.113.268303 PACS numbers: 82.70.Dd, 82.35.Rs, 87.14.gk

Charged polymeric layers densely attached by one end to an interface, also known as polyelectrolyte brushes, are systems that exhibit rich and complex behavior [1–7] with direct relevance to biological systems [8–11] and with a diverse range of applications such as surface modification technologies [10,12,13] and emerging biotechnologies [12,14,15]. Experimental observations of charged brushes available at present are not so sensitive to the details of the structure, but are mainly concerned with more global brush properties, such as brush thickness [16–18] or force-distance dependence between brushes [19–21]. However, the detailed picture of a polyelectrolyte brush comprises the determination of intramolecular density profiles and free-end arm distributions for the case of a dilute, noninteracting system. In the case of crowded conditions, additional parameters have to be quantified, namely, how the grafted charged coronas of brushes interact in terms of shrinkage, deformation, or penetration. In particular for the crowded case, many of the above-mentioned parameters are poorly accessible in a variety of physically distinct soft and penetrable colloidal systems [22–25]. In this Letter, we show how the above issues can be addressed by grafting very long double-stranded DNA (dsDNA) chains to the surface of a micron-sized spherical superparamagnetic particle for the construction of strongly charged, ultradense, highly monodisperse polyelectrolyte brushes with a star-shaped architecture (PE star). See the Supplemental Material [26] for details on the synthetic strategy, section 1.1–1.2.

Direct visualization of these water soluble DNA-based microstructures is achieved by fluorescent staining either the whole DNA chain [backbone labeling, (BL)] or only its free-end [free-end labeling, (FEL)]. In particular, the second labeling strategy allowed us to directly observe the internal structure of a PE star under highly crowded conditions, which is a significant improvement to existing visualization methods [33,34]. The above two labeling approaches are depicted schematically in Figs. 1(a)–1(b) together with their corresponding confocal fluorescent microscopy (CFM) images taken at their equatorial plane under dilute salt-free conditions (see Supplemental Material [26], section 1.3 for details on the labeling method, and the supporting movie shows the 3D reconstruction of a fluorescence free-end labeled PE star based on confocal microscopy sections). The corona thickness L of a PE star can be extracted from the azimuthally averaged radial fluorescent intensity of the above CFM images. Such a profile is shown in the top inset of Fig. 1(c) for the BL case. A power-law fit [Fig. 1(c)] of the thickness L, as extracted from the corresponding CFM images presented in Fig. 1(d), versus the arm length N for fixed f number of arms (termed functionality) yields $L \sim N$ under salt-free conditions. In addition, we find that L equals to the contour length L_c of the grafted dsDNA fragments, which indicates an extreme arm stretching while L is practically f independent over a wide range of arm lengths N [bottom inset of Fig. 1(c)]. This conformational behavior of the stars—owing to their ability to act as an efficient absorber of its own counterions under salt-free condition [2,35–38]—is in excellent agreement with the scaling predictions for an osmotic star [2,35].

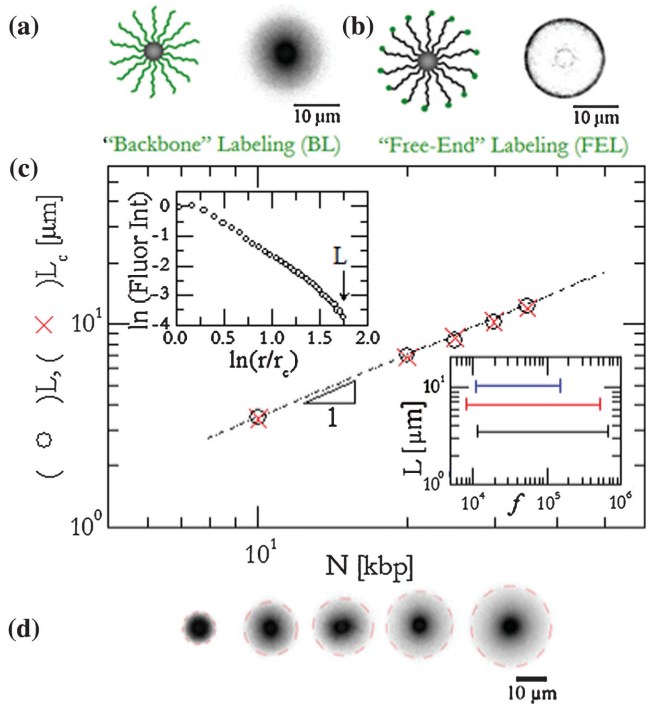

FIG. 1 (color). (a)–(b) Cartoon of the two fluorescent labeling strategies (shown in green) employed for the direct visualization of the DNA-based PE stars with their corresponding CFM images at their equatorial plane of particles (radius $r_c = 1.44$ μm) grafted with 3.0×10^5 dsDNA chains of 2.0×10^4 base pairs (bp). (c) Osmotic star corona thickness L (circles) versus the arm length N with $f = 1.4 \times 10^5$. Red crosses indicate the contour lengths L_c of the star arms. The line is the prediction of the scaling law for osmotic PE stars. Top inset: azimuthally averaged radial fluorescent intensity (normalized to the intensity on the surface of the star's core) versus the distance r (normalized to radius r_c of the core) from the center of a salt-free PE star with $f = 8.9 \times 10^4$ and $N = 20$ kbp. Bottom inset: the explored regions of functionalities where the star's corona thickness is independent of f (black, red, blue line: $N = 10$, 20, 30 kbp). (d) CFM images at the equatorial plane of the osmotic PE stars with $f = 1.4 \times 10^5$ and variable arm size (Left to right: $N = 10$, 20, 25, 30, 35 kbp). The red circles indicate the size of the PE star.

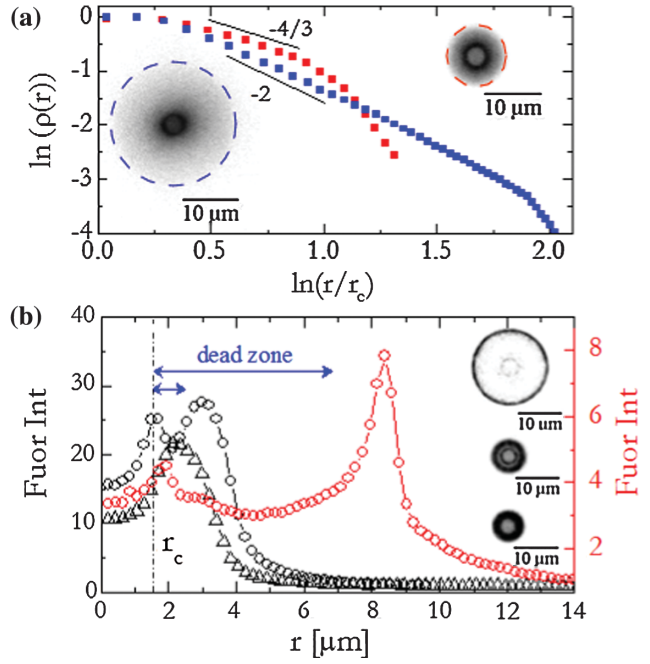

FIG. 2 (color). (a) DNA mass density profile $\rho(r)$ versus the distance r (normalized to radius r_c of star's core) from the center of a BL PE star with $f = 4.8 \times 10^4$ and $N = 30$ kbp under different salinity conditions together with their corresponding CFM images (salt-free: blue squares, bottom image and 0.1M NaCl: red squares, top image. The circles indicate the size of PE star). The bold lines show the slopes predicted by scaling. (b) The azimuthally averaged fluorescent intensity of CFM images of FEL PE star (normalized to the background fluorescent intensity) versus r for salt-free ($f = 5.14 \times 10^5$, $N = 20$ kbp, red circles, top image), 1.0M NaCl ($f = 5.14 \times 10^5$, $N = 20$ kbp, black circles, middle image), and 1.0M NaCl ($f = 1.31 \times 10^5$, $N = 20$ kbp, triangles, bottom image). The position of the surface of the star's core is indicated with a black line.

Information on the internal star structure is extracted from the azimuthally averaged mass density profile, which is directly related to the radial fluorescent intensity of the BL PE star [39]. A density profile is shown in Fig. 2(a) for an isolated osmotic (salt-free) PE star with $f = 4.8 \times 10^4$ and $N = 30$ kbp. Since the corona thickness follows the scaling $L \sim N$, the extension of the arms of the PE star is expected to be uniform. In a spherical geometry, this means that the radial distribution of the mass density in the star decays as r^{-2}, where r is the distance from the center of the star. Indeed, the slope of the measured profile in log-log representation is found to be very close to -2, supporting the picture of fully stretched chains having rodlike configuration [40–42,33]. By adding salt, the measured density profile reveals rearrangement of the intrinsic structure of the osmotic PE star. More specific, the significant deswelling of the PE star, as demonstrated in the CFM images [Fig. 2(a)], is accompanied by a change of the slope of the mass density profile from around -2 in the salt-free regime to $-4/3$ at relatively high salt concentration. The latter power law decay implies conformational behavior similar to a neutral star with enlarged (electrostatic) excluded volume, which has been predicted for the salted regime [41,43].

Complementary insight into the osmotic (salt-free) to salted regime transition can be obtained from the free-end distribution, as reflected from the azimuthally averaged radial fluorescent intensity of CFM images of FEL PE stars [Fig. 2(b), see also Supplemental Material [26], section 1.4 regarding the gradual nature of this transition as reflected from the changes in the size of the PE star]. While the free-end distribution confirms the thickness of the osmotic PE-star corona as found from the BL counterpart, it displays a maximum with narrow width, located at the periphery of the star [Fig. 2(b), red circles] with its position being virtually independent of the functionality. As a consequence, a region close to the center of the star is observed, where the free-ends are depleted ["dead zone", blue arrow, Fig. 2(b)].

By increasing the salt concentration, the free-end distribution becomes wider and its maximum moves to the center of the PE star [Fig. 2(b), black circles] indicating star shrinkage [see Supplemental Material [26], section 1.4 for more details]. Interestingly, the width of the dead zone relative to the size of the PE star decreases substantially with the addition of the salt and finally disappears for a lower functionality PE star [Fig. 2(b), triangles]. This is an additional verification for the similarity between neutral and highly salted stars, where excluded volume interactions play a dominant role in the equilibrium conformational structure of these macromolecular assemblies.

So far we focused on the conformational properties of an isolated PE star. We now consider PE-star accommodation scenarios under highly crowded conditions for star concentrations above the close packing fraction of spherical, undeformable objects with the same size as the isolated star. A simple and robust approach was employed for achieving tunable crowded conditions, utilizing a millimeter-sized square permanent magnet and taking advantage of the superparamagnetic properties of the star's core [Fig. 3(a), see also Supplemental Material [26], section 2.1 for more details]. Control over the magnet position h, thickness s of the sample holder and particle concentration provides an easy and robust way to organize the PE stars into two-dimensional (2D) hexagonal ordered arrays and, subsequently, compress them from an open [Fig. 3b] to space-filling configuration [Fig. 3(c)].

Visual inspection of Fig. 3(c) suggests that the space-filling lattice configuration is accompanied with the loss of the PE-star spherical symmetry and not by arm interpenetration. Unambiguous evidence is provided by the CFM image in Fig. 3(d), showing a compressed 2D crystal formed by osmotic PE stars ($f = 3.36 \times 10^5$ and $N = 20$ kbp) where a few FEL tracer PE stars are embedded in a host environment of unlabeled stars. A 2D hexagonal arrangement is achieved which is just space filling. This is verified by the sharp faceted labeled PE star, the relative position of star magnetic cores, and the fact that the distance L^* from the surface of the core to the vertices equals the corona radius of the undisturbed star L [inset of Fig. 3(d)]. The above observations indicate that the free ends are located near the facets with no observable interpenetration. The same behavior is even observed for stars with much lower functionality ($f = 4.1 \times 10^4$ and $N = 20$ kbp, see Supplemental Material [26], section 2.2.1).

The CFM images [Fig. 3(d) and Fig. S2 in the Supplemental Material [26]] provide direct evidence for noninterdigitation of the arms from different osmotic PE stars. Noninterdigitation is the main assumption of Pincus's theory [2], based on scaling arguments, on the interactions between PE stars which arises mainly from the entropic contribution of the trapped counterions [37]. In the salt-dominated regime for stars with low functionality ($f = 6.9 \times 10^4$) we do observe intra-arm penetration to some extent [Fig. 3(e), also see Supplemental Material [26], section 2.2.2]. However, in both cases the arms of two PE stars cannot penetrate more than the width of their free-end distribution. The latter observation has strong implications for using polyelectrolytes as a biomimetic lubrication agent between surfaces, since the degree of arm penetration controls entanglements, which in turn influence the friction between compressed PE stars.

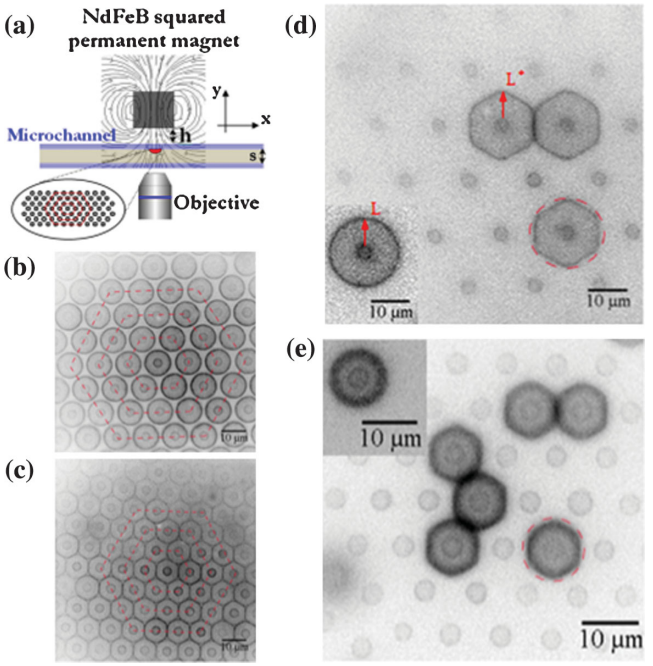

FIG. 3 (color). (a) Schematic diagram of the magnetic PE-star hexagonal array guidance system. (b)–(d), CFM images of 2D hexagonal lattice formed by the magnetically mediated self-assembly of FEL labeled PE stars with (b) open and (c)–(e) space filling configuration. (b)–(c) Osmotic stars with $f = 4.67 \times 10^5$ and $N = 10$ kbp. The red hexagons indicate the formation and homogeneous compression of the 2D PE-star lattice. (d) Osmotic stars with $f = 3.36 \times 10^5$ and $N = 20$ kbp. (e) Mild-salted (5 mM NaCl) stars with $f = 6.9 \times 10^4$ and $N = 20$ kbp. For (d)–(e) only a small fraction of PE stars are FEL labeled. The corresponding CFM images for an isolated PE star under the same salinity conditions are displayed in the insets. The red circles indicate the size of a PE star in the undisturbed state (see insets), where L is the corona thickness. L^* is the distance from the surface of the core of the hexagonal-shaped PE star to its vertex.

We estimate the pressures involved in the above compression experiments on the 2D hexagonal PE-star lattice by conducting osmotic stress experiments on an isolated salt-free PE star using neutral polymer dextran as an osmotic stress agent (see Supplemental Material [26], section 2.3). In particular, assuming that the radius of the incircle of the hexagonal compressed PE star is equivalent to the radius of an osmotic compressed PE star then the compression in Fig. 3(d) corresponds to a pressure of 8.5 kPa (red cross in Fig. S5 [26]). A higher degree of magnetically mediated PE-star compression has been achieved by employing a similar approach as the one depicted in Fig. 3(a), but now close to a water-air interface (see Supplemental Material [26], section 2.2.3). The results show a load carrying ability of the osmotically counterion

swollen PE stars without any detectable interpenetration of their arms at pressures well above the highest measurable osmotic pressure of 25 kPa. Therefore, our observations reveal that the osmotic pressure due to the trapped counterions inside the PE-star corona is indeed the primary mechanism for exceptional lubrication properties of polyelectrolyte brushes up to very high normal pressures as suggested in Refs. [5,10,44].

It is reasonable to hypothesize that a 2D PE-star crystal may be more tolerant to the inclusion of particles of different sizes given the PE-star deformability, stimuli responsiveness, and remarkable resistance to interpenetration of their charged coronas as they are packed more densely. This is in contrast to a 2D hard-sphere colloidal crystal [45] or any deformable but volume preserving system such as 2D bubble rafts [46]. The effects of the inclusion of a larger PE star are illustrated with the CFM image of Fig. 4(a). A 2D close-packed crystal under mild salinity conditions formed by FEL PE stars was doped with unlabeled larger PE stars with a volume 3.4 times that of

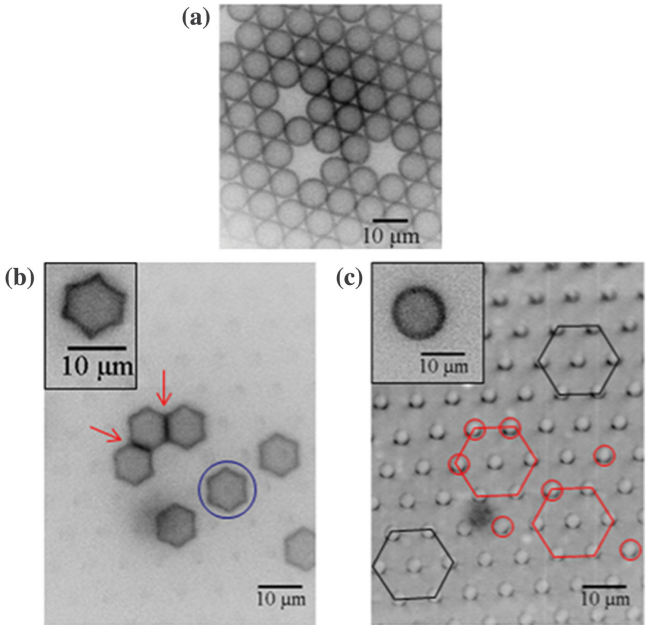

FIG. 4 (color). Confocal microscopy images of a close packed 2D hexagonal lattice formed by PE stars ($f = 3.1 \times 10^5$ and $N = 10$ kbp) that can tolerate the presence of larger foreign PE stars ($f = 3.91 \times 10^5$ and $N = 20$ kbp) under mild salinity conditions (5 mM NaCl). (a)–(b) CFM images where only the host or foreign PE stars are labeled (FEL), respectively. The blue circle indicates the size of an undisturbed doped star. Inset: an oversized doped PE star with highly curved edges. The red arrows point to the flat edges. (c) Bright-field image corresponding to the CFM image of (b), where only the magnetic cores of the PE stars (host and foreign) are visible. The red circles indicate the location of the foreign particles. Visual comparison of the black and red hexagons, which contain only host and a mixture of host and foreign PE stars, respectively, suggests that the crystal lattice is not affected by the presence of large particles. Inset: undisturbed foreign PE star.

the host particles. Interestingly, the oversized doped star fits into the host structure without causing local distortion of the crystal lattice. This is evidenced by a comparison of the CFM image of Fig. 4(b), where only the doped PE stars are labeled, with the corresponding bright-field confocal microscopy image in Fig. 4(c), where only the magnetic cores of the host and foreign particles are visible. Indeed, the doped particles adapt to their new local environment by becoming highly compressed and faceted as they are squeezed by neighboring PE stars. The final shape of the oversized foreign particles in the 2D crystal is dictated by the number and type of first nearest neighbors. Thus, in our case, the shape of the doped particle is found to be a hexagon with concave edges [Fig. 4(b) and inset] or a mixture of concave and flat edges [as indicated by arrows in Fig. 4(b)] depending on whether it is surrounded by only host or a mixture of host and doped particles, respectively.

Comparison of the foreign particle dimensions with and without confinement [blue circle in Fig. 4(b)] suggests that the doped particles adjust their volume not only because of direct interactions between the particles but also through a shrinking pathway. The latter mechanism was also reported in similar experiments performed on three-dimensional crystals made of micrometer-sized soft microgel particles, where this behavior is attributed solely to osmotic effects [47]. In our case, the ability to visualize local structural features with high resolution reveals that a delicate synergy exists between the osmotic pressure within each particle and the elastic deformation of its charged corona. Additional support has been obtained by exploring the role of salt and size ratio in the impurity tolerance of a 2D PE-star crystal. The results show the existence of a narrow window of parameters where the integration of a larger particle is possible (see Supplemental Material [26], section 2.4), stressing the role of softness of the interaction potential on the defect tolerance of our 2D hexagonal PE crystals. A rich phase behavior of PE-star solutions based on effective interactions [48] has been predicted and partially experimentally verified with SAXS measurements [49]. Our work suggests that a refinement of the models used for the predictions is at place, taking into account density-dependent particle shrinkage and deformation. This may reveal even more unusual phase behavior.

In summary, we have demonstrated an easy and robust route for the fabrication of ultradense long dsDNA-coated superparamagnetic particles. The resulting star-branched polyelectrolytes allow for the direct visualization of the internal structure, deformability, and interpenetrability of these model charged soft spheres under dilute and highly packed conditions at an unprecedented level of detail. Our results on their exceptional resistance to mutual interpenetration, at pressures approaching the MPa range, could be a great value for "*in situ*" study of tribological processes involving polymeric surfaces in aqueous environments. Moreover, our approach facilitates the simultaneous measurement of friction forces and direct visualization of the

brush, which could have a significant impact on the design of new biolubrication strategies [10,15].

The research was supported by the Transregio Sonderforschungsbereiche TR6018 "Physics of Colloidal Dispersions in External Fields."

*Corresponding author.
e.stiakakis@fz-juelich.de

[1] S. Misra, S. Varanasi, and P. P. Varanasi, Macromolecules **22**, 4173 (1989).
[2] P. Pincus, Macromolecules **24**, 2912 (1991).
[3] O. V. Borisov, E. B. Zhulina, and T. M. Birshtein, Macromolecules **27**, 4795 (1994).
[4] M. Ballauff and O. V. Borisov, Curr. Opin. Colloid Interface Sci. **11**, 316 (2006).
[5] J. B. Sokoloff, J. Chem. Phys. **129**, 014901 (2008).
[6] A. Jusufi and C. N. Likos, Rev. Mod. Phys. **81**, 1753 (2009).
[7] O. V. Borisov, E. B. Zhulina, F. A. M. Leemakers, M. Ballauff, and A. H. E. Müller, Adv. Polym. Sci. **241**, 1 (2011).
[8] E. B. Zhulina and F. A. M. Leemakers, Soft Matter **5**, 2836 (2009).
[9] A. Dėdinaitė, Soft Matter **8**, 273 (2012).
[10] A. Raviv, S. Giasson, N. Kampf, J. F. Gohy, R. Jérôme, and J. Klein, Nature (London) **425**, 163 (2003).
[11] S. S. Daube, D. Bracha, A. Buxboim, and R. H. Bar-Ziv, Proc. Natl. Acad. Sci. U.S.A. **107**, 2836 (2010).
[12] A. Wittemann, B. Haupt, and M. Ballauff, Phys. Chem. Chem. Phys. **5**, 1671 (2003).
[13] F. Zhou, P. M. Biesheuvel, E. Y. Choi, W. Shu, R. Poetes, U. Steiner, and W. T. Huck, Nano Lett. **8**, 725 (2008).
[14] D. J. Lockhart, H. Dong, M. C. Byrne, M. T. Follettie, M. V. Gallo, M. S. Chee, M. Mittmann, C. Wang, M. Kobayashi, H. Horton, and E. L. Brown, Nat. Biotechnol. **14**, 1675 (1996).
[15] T. Moro, Y. Takatori, K. Ishihara, T. Konno, Y. Takigawa, T. Matsushita, U. Chung, K. Nakamura, and H. Kawaguchi, Nat. Mater. **3**, 829 (2004).
[16] R. Hariharan, C. Biver, J. Mays, and W. B. Russel, Macromolecules **31**, 7506 (1998).
[17] X. Guo and M. Ballauff, Phys. Rev. E **64**, 051406 (2001).
[18] A. S. Lee, V. Bütün, M. Vamvakaki, S. P. Armes, J. A. Pople, and A. P. Gast, Macromolecules **35**, 8540 (2002).
[19] K. Kegler, M. Konieczny, G. Dominguez-Espinoza, C. Gutsche, M. Salomo, F. Kremer, and C. N. Likos, Phys. Rev. Lett. **100**, 118302 (2008).
[20] G. Dominguez-Espinoza, A. Synytska, A. Drechsler, C. Gutsche, K. Hegler, P. Uhlmann, M. Stamm, and F. Kremer, Polymer **49**, 4802 (2008).
[21] F. Huang, K. Addas, A. Ward, N. T. Flynn, E. Velasco, M. F. Hagan, Z. Dogic, and S. Fraden, Phys. Rev. Lett. **102**, 108302 (2009).
[22] C. M. Hui, J. Pietrasik, M. Schmitt, C. Mahoney, J. Choi, M. R. Bockstaller, and K. Matyjaszewski, Chem. Mater. **26**, 745 (2014).
[23] J. Roovers, Macromolecules **27**, 5359 (1994).
[24] J. Buitenhuis and S. Förster, J. Chem. Phys. **107**, 262 (1997).
[25] H. Senff and W. Richtering, J. Chem. Phys. **111**, 1705 (1999).
[26] See Supplemental Material at http://link.aps.org/supplemental/10.1103/PhysRevLett.113.268303, which includes Refs. [27–32].
[27] K. Kegler, M. Salomo, and F. Kremer, Phys. Rev. Lett. **98**, 058304 (2007).
[28] A. Buxboim, S. S. Daube, and R. Bar-Ziv, Nano Lett. **9**, 909 (2009).
[29] C. Carlsson, M. Johnson, and B. Akerman, Nucleic Acids Res. **23**, 2413 (1995).
[30] A. L. Gassner, M. Abonnenc, H. X. Chen, J. Morandini, J. Josserand, J. S. Rossier, J. M. Busnel, and H. H. Girault, Lab Chip **9**, 2356 (2009).
[31] F. R. Senti, N. N. Hellman, N. H. Ludwig, G. E. Babcock, R. Tobin, C. A. Glass, and B. L. Lamberts, J. Polym. Sci. **17**, 527 (1955).
[32] V. A. Parsegian, R. P. Rand, N. L. Fuller, and D. C. Rau, Methods Enzymol. **127**, 400 (1986).
[33] A. Wittemann, M. Drechsler, Y. Talmon, and M. Ballauff, J. Am. Chem. Soc. **127**, 9688 (2005).
[34] F. A. Plamper, A. Walther, A. H. E. Müller, and M. Ballauff, Nano Lett. **7**, 167 (2007).
[35] O. V. Borisov, J. Phys. II (France) **6**, 1 (1996).
[36] M. Roger, P. Guenoun, F. Muller, L. Belloni, and M. Delsanti, Eur. Phys. J. E **9**, 313 (2002).
[37] A. Jusufi, C. N. Likos, and H. Löwen, J. Chem. Phys. **116**, 11011 (2002).
[38] F. A. Plamper, H. Becker, M. Lanzendörfer, M. Patel, A. Wittemann, M. Ballauff, and A. H. E. Müller, Macromol. Chem. Phys. **206**, 1813 (2005).
[39] Our CCD camera is nonintensified, allowing for a linear relationship between the intensity of light impinging on a pixel and the final value of the digital intensity in the acquired image. Since the BL labeling method involves intercalation of fluorescent dye, which is insensitive to base pair sequence, it is valid to assume that the fluorescent intensity is linearly related with DNA mass at a particular image location. Therefore, the fluorescent intensity decay can be directly related to the radial dependence of the star mass density profile.
[40] O. V. Borisov and E. B. Zhulina, J. Phys. II (France) **7**, 449 (1997).
[41] O. V. Borisov and E. B. Zhulina, Eur. Phys. J. B **4**, 205 (1998).
[42] P. Guenoun, F. Muller, M. Delsanti, L. Auvray, Y. J. Chen, J. W. Mays, and M. Tirell, Phys. Rev. Lett. **81**, 3872 (1998).
[43] J. Klein Wolterink, F. A. M. Leermakers, G. J. Fleer, L. K. Koopal, E. B. Zhulina, and O. V. Borisov, Macromolecules **32**, 2365 (1999).
[44] U. Raviv, S. Giasson, N. Kampf, J. F. Gohy, R. Jérôme, and J. Klein, Langmuir **24**, 8678 (2008).
[45] D. R. Nelson, M. Rubinstein, and F. Spaepen, Philos. Mag. A **46**, 105 (1982).
[46] L. Bragg and J. F. Nye, Proc. R. Soc. A **190**, 474 (1947).
[47] A. S. Iyer and A. L. Lyon, Angew. Chem. Intl. Ed. **48**, 4562 (2009).
[48] N. Hoffmann, C. N. Likos, and H. Löwen, J. Chem. Phys. **121**, 7009 (2004).
[49] T. Furukawa and K. Ishizu, Macromolecules **38**, 2911 (2005).